13th IEA Heat Pump Conference
April 26-29, 2021 Jeju, Korea

Numerical investigation on PCM-to-refrigerant heat exchangers for thermal energy storage

Yiyuan Qiao[a], Tao Cao[a], Yunho Hwang[a,*], Jiazhen Ling[a], Vikrant Aute[a]

[a] Center for Environmental Energy Engineering, Department of Mechanical Engineering, University of Maryland, 4164 Glenn Martin Hall Bldg., College Park, MD 20742, United States

Abstract

Recently, the application of thermal energy storage systems using phase change materials (PCM) is expanding in many fields due to the high energy storage density of PCMs and the narrow phase-change temperature range. In this paper, we conducted a numerical investigation on a shell-and-tube configured PCM-to-refrigerant heat exchanger (PCMHX) coupled in a vapor compression cycle for personal cooling. The enthalpy method was applied to the phase change analysis. The finite-volume method was employed to address the two-dimensional PCMHX numerical solution. Different from most of the previous studies on PCM-to-water heat exchangers, the proposed PCMHX works as a condenser. We validated the simulation results against the experiment data, including condenser pressure, capacity, and PCM temperature profiles. Since the refrigerant-side heat transfer coefficient changes along the condenser length, the heat transfer flux is not uniform across the PCM. Therefore, we analyzed the uneven PCM melting and its effects on the condensing temperature. Results show that PCM near the condenser outlet melts slower than other sections because of the low heat transfer coefficient and small temperature difference in a subcooled liquid region. The developed PCMHX model can reasonably predict the time-dependent heat transfer performance and the PCM melting process.

Selection and/or peer-review under responsibility of the organizers of the 13th IEA Heat Pump Conference 2020.

Keywords: Modeling; Phase change; PCM-to-refrigerant heat exchanger; Thermal energy storage; Enthalpy method

Nomenclature			
A, A'	heat transfer area (mm^2)	cond	condenser
C	specific heat ($kJ \cdot kg^{-1} \cdot K^{-1}$)	dia	diaphragm of TXV
C_v	flow coefficient (--)	evap	evaporator
h	enthalpy ($kJ \cdot kg^{-1}$)	fin	fin
H	latent heat ($kJ \cdot kg^{-1}$)	i	inner
i, j	segment number	in	inlet
k	thermal conductivity ($W \cdot m^{-1} \cdot K^{-1}$)	ini	initial
K	spring constant ($N \cdot m^{-1}$)	isen	isentropic
L	length of the PCM cylinder (mm)	l	liquid phase
Le	Lewis number (--)	m	melting, motor
m	mass (kg)	o	outer
$\dot{m}$	mass flow rate ($g \cdot s^{-1}$)	out	outlet
N	rotational speed (rpm)	p	PCM
P	pressure (kPa)	r	radial direction
r, R	radius (mm)	ref	refrigerant
t	time (s)	s	solid phase

* Corresponding author. Tel.: +1-301-405-5247.
E-mail address: yhhwang@umd.edu.

T	temperature (°C)	t	tube
W	power consumption (W)	top	top
y	deflection of spring in TXV (m)	th	throttle of TXV
z	length in z direction (mm)	vol	volumetric
		w	wall
Greek symbols		z	axial direction
α	heat transfer coefficient ($W \cdot m^{-2} \cdot K^{-1}$)		
η	efficiency	Abbreviations	
ρ	density ($kg \cdot m^{-3}$)	CENG	compressed expanded natural graphite
λ	liquid fraction (--)	COP	coefficient of performance
δ	thickness of wall (mm)	MCHX	micro-channel heat exchanger
ω	humidity ratio ($kg \cdot kg^{-1}$)	MFM	mass flow meter
		PCM	phase change material
Subscripts		PCMHX	PCM heat exchanger
A	ambient	TXV	thermostatic expansion valve
b	bulb sensor of TXV	VCC	vapor compression cycle
comp	compressor		

1. Introduction

Phase change material (PCM) coupled heat exchangers are attracting more attention recently since PCM can absorb or release heat within a narrow temperature range. Most PCMHX (PCM heat exchangers) models were developed by commercial CFD software and only a few through self-developed programming [1]. The two most common numerical methods can be used to build the PCM numerical heat transfer model: (1) enthalpy method, (2) effective heat capacity method [1,2]. In the enthalpy method, by introducing enthalpy, the phase change process can be much more straightforward. Latent heat and sensible heat are combined as the enthalpy in the energy equation to avoid nonlinearity in the heat conduction problem [3]. The governing equation is the same for the liquid phase, mushy phase, and solid phase. The melting interface conditions are automatically achieved by evaluating the PCM enthalpy [2,4]. Most PCMs are not pure, and thus phase change occurs over a range of temperatures rather than at a constant temperature. In this paper, a vapor compression cycle (VCC) coupled with PCM through PCMHX was proposed and modeled. The proposed system could be used as a personal cooling system [5,6], in which PCMHX worked as a condenser to store the waste heat to avoid dumping heat to the ambient and reducing human comfort. The enthalpy method was applied to develop the transient model of the refrigerant-to-PCM heat exchanger. We validated the transient VCC system model and PCMHX model against the experimental results, and PCMHX heat transfer characteristics and system performance were also analyzed and discussed in this study.

2. System description

The PCM coupled VCC system can be used as a personal cooling system. Using the personal cooling system, the thermal state setting of the building can be higher to reduce the building energy consumption, and meanwhile, occupants can feel comfortable with the localized cooling. The schematic diagram of VCC coupled with PCM through PCMHX is illustrated in Fig. 1(a), in which PCMHX works as a condenser in the VCC system to store the waste heat from refrigerant condensation. So that the heat is not to the ambient and cannot reduce the human comfort. Therefore, the whole system including the PCMHX can be assembled together on a robotic base and powered by an electric battery to achieve the movability in buildings. The air-to-refrigerant evaporator is used for providing personal cooling in the VCC-based system. A more comprehensive system experimental investigation could be found in [5]. PCMHX was designed with multiple parallel tubes with the refrigerant flowing inside tubes and PCM was filled in the annular space between PCM container and tubes as illustrated in Fig. 1(b). R134a worked as a refrigerant flowing vertically downward. Paraffin/graphite was selected as the PCM composite, in which paraffin was immersed inside the compressed, expanded natural graphite (CENG) matrix. A refrigerant distribution header and collection header were installed at the top and bottom of PCMHX, respectively, in which the refrigerant was assumed to be uniformly distributed to eight copper branch tubes. PCMHX specifications are listed in Table 1.

3. PCM condenser model

A segment-by-segment condenser model was developed for the PCMHX. Assumptions of the PCMHX model used were: (1) radiation heat to the surrounding was neglected, (2) refrigerant conduction, viscous dissipation, kinetic energy, and potential energy were neglected, (3) only thermal conduction in the CENG matrix was considered, and the effective thermal conductivity was different in the axial and radial directions, (4) the specific heat of PCM was different for the solid and liquid phases, and (5) a unit of a single tube and PCM cylinder can represent the heat transfer performance of original eight-tube PCMHX design. Fig. 1(c) is the single tube unit. To keep the same mass of PCM per tube, the cross-section of the single-tube unit was 1/8 of the original cross-section. To maintain the same heat transfer area per tube, the tube length of the single unit (L) was the same as the eight-tube design. Paraffin wax, PureTemp37, was selected as the PCM with a melting temperature of 37°C. The thermal properties of PureTemp37 are listed in Table 2.

Table 1: PCMHX design properties

Parameters	Unit	Value
PCM container diameter	mm	265
PCM composite height	mm	280
Tube length	mm	300
Tube without PCM length	mm	20
Numbers of tubes	--	8
Tube inside diameter	mm	4.8
Tube outside diameter	mm	6.4
Header length	mm	51.8
Header inside diameter	mm	7.9
Header outside diameter	mm	9.5

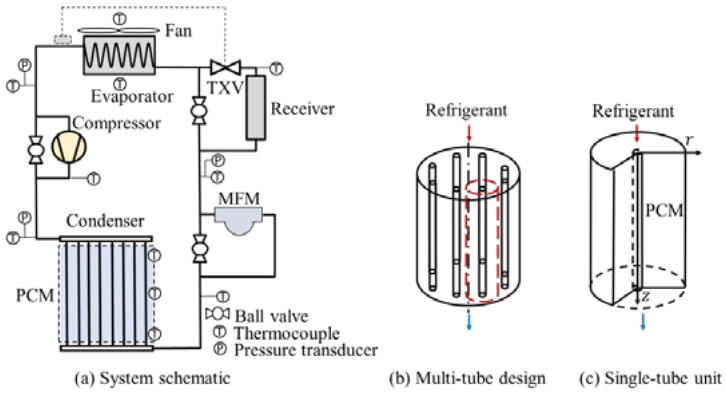

Fig. 1. PCMHX design and modeling unit (TXV: thermostatic expansion valve. MFM: mass flow meter).

Table 2. Properties of PureTemp37

Properties	Unit	Value
Melting temperature	°C	36.5~37.5
Latent heat	kJ·kg^{-1}	210
Thermal conductivity	W·m^{-1}·K^{-1}	0.15 (liquid), 0.25 (solid)
Density	kg·m^{-3}	840 (liquid), 920 (solid)
Specific heat	kJ·kg^{-1}·K^{-1}	2.63 (liquid), 2.21 (solid)

3.1. PCM side model

Under the cylindrical coordinate system, there is a rotation symmetric heat transfer to PCM with respect to the longitudinal axis (see Fig. 1(c)). Therefore, a transient two-dimensional (2D) numerical model was used to simulate heat transfer and PCM melting process in the PCM condenser. The enthalpy method was adopted for the 2-D PCM modeling. The energy equation is given by Eq. (1). T_p and h_p are PCM temperature and enthalpy, respectively. h_p is a function of PCM temperature. $k_{p,r}$ and $k_{p,z}$ are PCM effective thermal conductivity in radial direction and axial direction, respectively. PCM enthalpy and effective thermal conductivity are two crucial parameters that need to be determined to solve this energy equation.

$$\rho_p \frac{\partial h_p}{\partial t} = k_{p,r} \frac{1}{r} \frac{\partial}{\partial r}\left(r \frac{\partial T_p}{\partial r}\right) + k_{p,z} \frac{\partial^2 T_p}{\partial z^2} \tag{1}$$

PCM liquid fraction is given by Eq. (2) to evaluate the PCM melting process. T_s and T_l are PCM temperatures at the beginning and the end of the phase change process, respectively.

$$\lambda(T_p) = \begin{cases} 0 & h \le h_s \\ \dfrac{T_p - T_s}{T_l - T_s} & h(T_s) < h < h(T_l) \\ 1 & h \ge h_l \end{cases} \tag{2}$$

The PCM effective thermal conductivity in the radial direction, $k_{p,r}$, and that in the axial direction, $k_{p,z}$ are significant parameters to address this numerical problem as in Eq. (1). $k_{p,r}$ and $k_{p,z}$ are different due to the manufacturing process of PCM/CENG composite [7]. The thermal conductivity of the CENG matrix in the compression force direction is less than the perpendicular direction. The correlations used for effective conductivities $k_{p,r}$ and $k_{p,z}$ are proposed by Py et al. [8].

Boundary conditions for PCM temperature are given in Eqs. (3) to (6). R_i is the inner radius of the PCM cylinder, which is the same as the tube outer radius. R_o and L are the outer radius of the single-tube unit and the cylinder length, respectively. A_i and A_{top} is the heat transfer area contacted tube walls and the top area of the PCM cylinder, respectively. A_o is the equivalent outer heat transfer area for the single-tube unit to the surrounding. $A_o = A_o'/8$, in which A_o is the outer surface area of the original multi-tube design. α_1, α_2 and α_3 are the natural convection heat transfer coefficient at the outer, top and bottom boundary, which are calculated by the correlation proposed by [9]. T_a and T_w are the surrounding and wall temperatures, respectively.

$$k_{p,r} \frac{\partial T_p(r,z,t)}{\partial r} = A_i \frac{2k_w}{\delta}\left(T_w(z,t) - T_p(r,z,t)\right) \quad r = R_i \tag{3}$$

$$k_{p,r} \frac{\partial T_p(r,z,t)}{\partial r} = \alpha_1 A_o\left(T_p(r,z,t) - T_a\right) \quad r = R_o \tag{4}$$

$$k_{p,z} \frac{\partial T_p(r,z,t)}{\partial r} = \alpha_2 A_{top}\left(T_p(r,z,t) - T_a\right) \quad z = 0 \tag{5}$$

$$k_{p,z} \frac{\partial T_p(r,z,t)}{\partial r} = \alpha_3 A_{top}\left(T_p(r,z,t) - T_a\right) \quad z = L \tag{6}$$

The initial condition for PCM temperature is as follows:

$$T_p(r,z,t) = T_{ini} \quad t = 0 \tag{7}$$

A finite-volume method was adopted to solve the aforementioned governing equations for PCM. As illustrated in Fig. 2, uniform segments were applied for the discretization along with axial and radial directions in the PCM domain. Control volumes in the axial and radial directions are designated by *i* and *j*. Each PCM control volume is an annular space. The discretized energy equation for PCM heat transfer using the enthalpy method is given in Eq. (8). $A_{p,r}$ and $A_{p,z}$ are the heat transfer areas of each control volume in the radial direction and axial direction, respectively.

$$m_{p_{(i,j)}}\frac{h_{p_{(i,j)}}}{\partial t}=\frac{k_{p,r}}{dr}A_{p,r_{(j)}}\left(T_{p_{(i,j-1)}}-T_{p_{(i,j)}}\right)-\frac{k_{p,r}}{dr}A_{p,r_{(j+1)}}\left(T_{p_{(i,j)}}-T_{p_{(i,j+1)}}\right)+\frac{k_{p,z}}{dz}A_{p,z_{(j)}}\left(T_{p_{(i-1,j)}}-T_{p_{(i,j)}}\right)-\frac{k_{p,z}}{dz}A_{p,z_{(j)}}\left(T_{p_{(i,j)}}-T_{p_{(i+1,j)}}\right) \quad (8)$$

3.2. Refrigerant side model

The refrigerant flow was one-dimensional, and the conduction term was neglected. The energy equation and continuity equations of the refrigerant flow are given in Eqs. (9) and (10), respectively. Pressure (P) and specific enthalpy (h) were selected as state variables [10,11]. Refrigerant properties including density, ρ, the partial derivative of density with respect to enthalpy, $(d\rho/dh)|_p$, and that with respect to pressure, $(d\rho/dP)|_h$, were obtained by refrigerant property functions proposed in [12].

$$\frac{dU}{dt}=\mathrm{V}\left[\left(h\left.\frac{d\rho}{dP}\right|_h-1\right)\frac{dP}{dt}+\left(h\left.\frac{d\rho}{dh}\right|_p+\rho\right)\frac{dh}{dt}\right] \quad (9)$$

$$\frac{dm}{dt}=\mathrm{V}\left(\left.\frac{d\rho}{dP}\right|_h\frac{dP}{dt}+\left.\frac{d\rho}{dh}\right|_p\frac{dh}{dt}\right) \quad (10)$$

As shown in Fig. 2, spatial discretization along the axial direction was adopted for the refrigerant flow as well. Discretized energy and continuity equations for the refrigerant are given in Eqs. (11) and (12), respectively. h_{in} and h_{out} are refrigerant enthalpy flowing into and out of the selected cross section. $\dot{m}_{in}$ and $\dot{m}_{out}$ are refrigerant mass flow rate flowing into and out of the selected section. α_{ref} is the convective heat transfer coefficient. For single-phase flow, α_{ref} is calculated from correlations proposed in [13]. For two-phase flow, α_{ref} calculation was based on the correlation in [14]. α_{ref} of two-phase flow changes with quality x, and the smooth function was used at $x < 0.05$ and $x > 0.95$ to prevent discontinuities of the heat transfer coefficient at the phase transition point.

$$V_{(i)}\left(\left.\frac{d\rho}{dP}\right|_{h_{(i)}}\frac{dP}{dt}_{(i)}+\left.\frac{d\rho}{dh}\right|_{p_{(i)}}\frac{dh}{dt}_{(i)}\right)=\dot{m}_{(i)}-\dot{m}_{(i+1)} \quad (11)$$

$$V_{(i)}\left[\left(h(i)\left.\frac{d\rho}{dP}\right|_{h_{(i)}}-1\right)\frac{dP}{dt}_{(i)}+\left(h(i)\left.\frac{d\rho}{dh}\right|_{p_{(i)}}+\rho_{(i)}\right)\frac{dh}{dt}_{(i)}\right]=\dot{m}_{(i)}h_{(i)}-\dot{m}_{(i+1)}h_{(i+1)}+\alpha_{ref(i)}A_{p,r_{(1)}}(T_{HTF\,(i)}-T_{w(i)}) \quad (12)$$

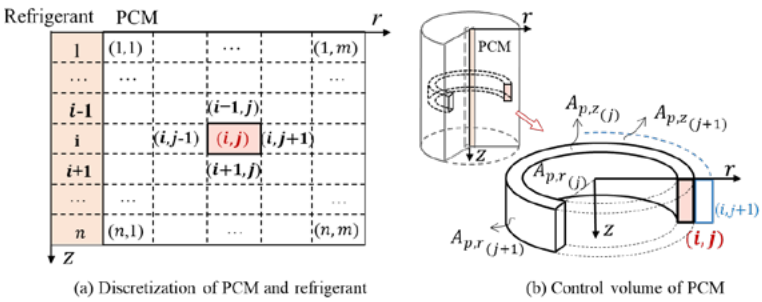

(a) Discretization of PCM and refrigerant (b) Control volume of PCM

Fig. 2. Discretization of PCMHX

4. Other component models

Different from most of the previous studies on water-to-PCM heat exchangers, in this paper, the refrigerant flowing inside PCM tubes is the refrigerant. Since PCM temperature profiles vary during the melting process, and affect the PCMHX performance, and thus for the VCC the refrigerant inlet states and heat transfer coefficient along the flow direction vary with time in the PCMHX. This variation can also be reflected by Eq. (3), showing that the PCM boundary condition at R_i is neither the constant heat flux nor the constant wall temperature. Therefore, to simulate the PCMHX performance, the VCC system should be modeled. Components include an evaporator, thermostatic expansion valve (TXV), compressor, receiver, and pipes.

4.1. Evaporator model

A fin-and-tube heat exchanger was selected as the evaporator design. Discretized governing equations of refrigerant in evaporator are the same as those in the PCM condenser, as described in Eqs. (11) and (12). Heat transfer coefficient of refrigerant, α_{ref}, was calculated using correlations propose by [15] for two-phase flow and by [13] for single-phase flow. For tube wall and fins, the energy equation is given by Eq. (13).

$$\begin{aligned}\left(M_w C_{p,w} + M_{fin} C_{p,fin}\right)\frac{dT_w}{dt} \\ = \alpha_{ref} A_{ref}\left(T_w - T_{ref}\right) + \dot{m}_a C_{p,a}\left(T_{a,in} - T_{a,out}\right) + \dot{m}_a H_a(\omega_{a,in} - \omega_{a,out})\end{aligned} \tag{13}$$

In Eq. (13), the first term at the right-hand side is the heat transfer between tube walls and refrigerant, the second term means sensible heat released from air to tube walls, and the third term is the latent heat from the air. $\dot{m}_a$, $C_{p,a}$ and H_a are air mass flow rate, air specific heat, and water vaporization heat, respectively. $T_{a,in}$, $T_{a,out}$, $\omega_{a,in}$ and $\omega_{a,out}$ are air inlet temperature, outlet temperature, inlet humidity ratio and outlet humidity ratio, respectively. $T_{a,in}$ and $\omega_{a,in}$ are known. $T_{a,out}$ and $\omega_{a,out}$ can be solved by Eqs. (14) and (15), yielding air side governing equations as described by [10].

$$T_{a,out} = T_{a,in} + (T_w - T_{a,in})\left\{1 - exp\left[-\frac{\alpha_a\left(A_t + \eta_{fin}A_{fin}\right)}{\dot{m}_a C_{p,a}}\right]\right\} \tag{14}$$

$$\omega_{a,out} = \omega_{a,in} + \left\{1 - exp\left[-\frac{\alpha_a\left(A_t + \eta_{fin}A_{fin}\right)}{\dot{m}_a C_{p,a} Le^{2/3}}\right]\right\} min\left(0, \omega_{a,sat} - \omega_{a,in}\right) \tag{15}$$

A_t and A_{fin} are heat transfer area of tube-side and fin-side, respectively. Fin efficiency, η_{fin} was calculated using correlations proposed by [16]. Airside heat transfer is enhanced by plate wavy-herringbone fins with a staggered tube layout. Thus, the air-side heat transfer coefficient, α_a, was obtained from the correlations proposed by [17]. *Le* is the Lewis number yielding $Le^{2/3}$=0.9 [18].

4.2. TXV model

The TXV model is described in [10] and [19]. TXV was assumed to be adiabatic. The expansion of the refrigerant was assumed to be isenthalpic. The refrigerant mass flow rate controlled by the TXV is given by Eq. (16), in which C_v is the flow coefficient, A_t is the flow area of the throttle, Δp is the pressure drop across the valve.

$$\dot{m} = C_v A_t (\rho_{in} \Delta p)^{1/2} \tag{16}$$

The refrigerant flow area was controlled by a needle movement, which reflects the superheat degree at the evaporator outlet. Valve geometry and a function to obtain the TXV bulb temperature are presented in [10]. The force balance on the diaphragm is given in Eq. (17). The sensor provides a force on the one side of the diaphragm, $P_b A_{dia}$, which is the same with the total forces on the other side supplied by evaporator pressure and the spring. k_{sp}, y_{sp} and $F_{sp,ini}$ are the spring constant, deflection and the initial force, respectively.

$$k_{sp} y_{sp} + F_{sp,ini} + P_{evap} A_{dia} = P_b A_{dia} \tag{17}$$

4.3. Compressor model

The compressor provides a refrigerant mass flow throughout the VCC. The efficiency-based compressor model was applied in this study. Volumetric efficiency, η_{vol}, isentropic efficiency, η_{isen} and motor efficiency, η_m, were used to calculate the compressor power consumption, W_{comp}, as given in Eqs. (18) to (20). $\dot{m}$ and N are the mass flow rate and compressor speed, respectively. ρ_{in} is the refrigerant density at the inlet of the compressor.

$$h_{out} = h_{in} + \frac{h_{out,s} - h_{in}}{\eta_{isen}} \tag{18}$$

$$\dot{m} = \frac{\eta_{vol}\rho_{in}V_{comp}N}{60} \tag{19}$$

$$W_{comp} = \dot{m}\frac{h_{out} - h_{in}}{\eta_m} \tag{20}$$

4.4. Receiver and pipe models

The receiver model and connecting pipe model are essentially the same as the evaporator model. As described before, the refrigerant side can be solved by discretized equations as in Eqs. (11) and (12). The air-side heat transfer was based on natural convection.

5. Results

5.1. Grid sensitivity

Sensitivities to grid size and aspect ratio were investigated. The model was simulated under different grid sizes and aspect ratios as follows: 40x20, 30x10, 20x10, 10x5, and 5x5. Results are shown in Fig. 3. The deviation of both pressure and capacity between grids 40x20 and 30x10 is less than 1.0%. Therefore, the grid of 30x10 was good enough to be adopted in the simulation.

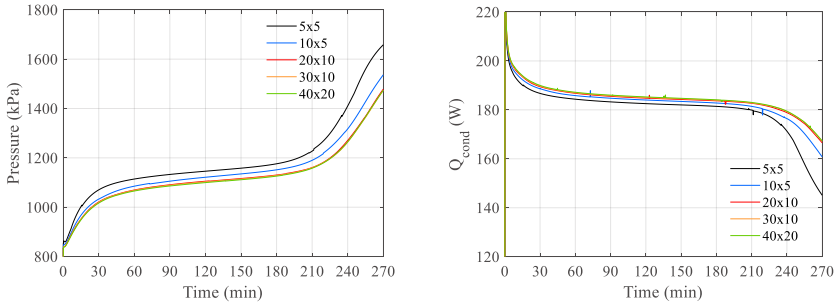

(a) Condenser pressure

(b) PCM condenser capacity

Fig. 3. Grid independence of numerical solution.

The PCMHX model and system model were developed in Dymola®. The algorithm of Lsodar was adopted, which is an implicit multi-step method. The backward differentiation formula was applied in the algorithm to solve differential equations. Time step size was determined on every step with a tolerance of $1e^{-6}$.

5.2. Simulation results

Fig. 4 (a)-(e) show the comparison of the experimental and numerical results on system operating pressures, condenser outlet subcooling and evaporator outlet superheat, mass flow rate, COP, and heat exchanger capacities indicating that numerical results match well with the experimental results. The good agreements illustrate that the numerical model is reliable. Fig. 4(f) shows the PCM temperatures at 1/3 from the top and bottom of the PCMHX for both numerical and experimental results. From Fig. 4(a), evaporating pressure was

almost constant due to the steady surrounding temperature. The condenser pressure increased with the cooling time due to the process of PCM melting. As the PCM absorbed heat from the condenser tube, its average temperature increased (Fig. 4(f)) and thus the condensing temperature was increased, leading to the increased of subcooling at the condenser outlet as well. Fig. 4(c) indicates mass flow rate decreased gradually, which is because the higher condensing pressure led to lower volumetric efficiency. Fig. 4(d) and (e) show the slightly decreased COP and capacity due to the increase of the condensing pressure. As can be seen from Fig. 4(f), the proposed PCMHX model can predict the PCM melting process well.

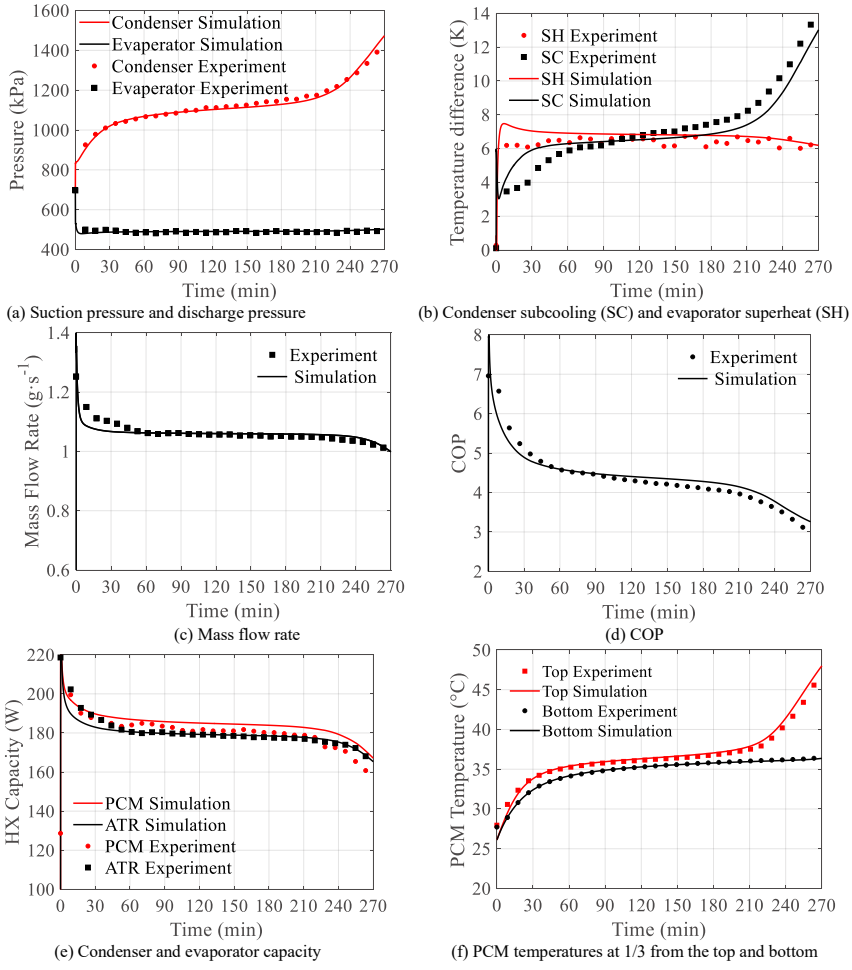

Fig. 4. Numerical results compared with experimental results.

Fig. 5 and Fig. 6 shows the numerical solution of the PCM temperature and melting fraction of the single-tube unit. The vertical direction means the condenser length direction, and the horizontal direction represents the radial direction. Refrigerant flowed downward from the top to the bottom. It can be found that the PCM melting rate decreased along the condenser length direction. The bottom PCM temperature was lower than the top and middle sections, which can also be verified by Fig. 4(f). The PCM temperature gradient in the radial direction was smaller than the axial direction. Besides, the heat transfer area of subcooled-liquid refrigerant increased with the cooling time. The refrigerant liquid zone at the bottom was greater than the vapor zone at the top near the condenser inlet. From Fig. 6, at 270 minutes, liquid fractions at the top 1/3 were higher than 0.9, while at the bottom 1/3 PCM liquid fractions were less than 0.4. This uneven PCM melting is due to the

uneven refrigerant heat transfer coefficient. At the top and middle section, the refrigerant-side heat transfer coefficient is much higher than that at the bottom because the refrigerant is in two-phase at the top and middle, while it becomes sub-cooled liquid at the bottom. It can be concluded that the utilization ratio of the PCM latent heat needs to be improved.

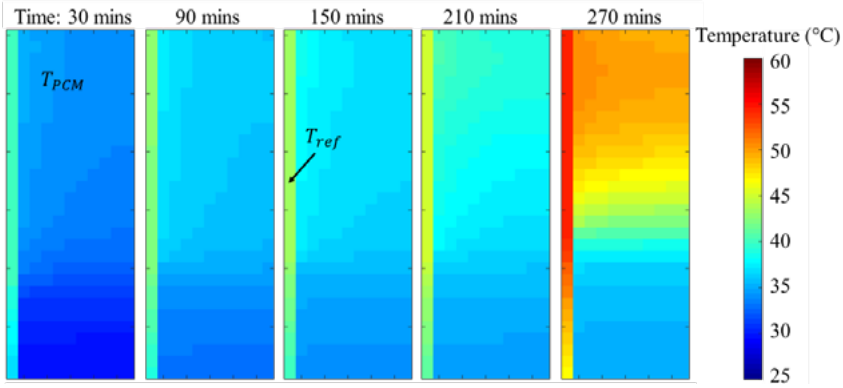

Fig. 5 PCM and refrigerant temperatures

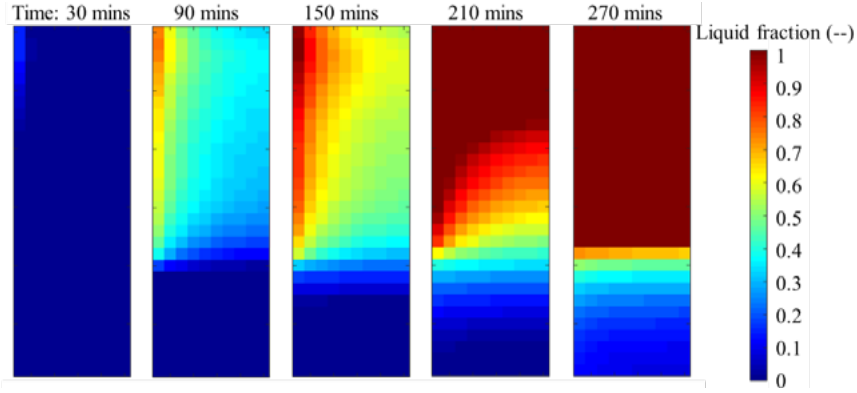

Fig. 6. PCM liquid fractions

Conclusions

In this paper, we developed the two-dimensional PCM-to-refrigerant heat exchanger model and transient system model of the VCC coupled with PCMHX in a personal cooling system. PCMHX works as a condenser of the VCC system and interface for thermal energy storage. Grid size sensitivity was checked, and numerical results were compared with the experimental results. It shows good agreements between simulation and experiment for both system performance and PCM heat transfer characteristics. Uneven PCM melting was also observed and reasoned due to the uneven heat transfer rate from the refrigerant to PCM along the condenser length. Therefore, a better PCMHX design should be further investigated to fully utilize the advantage of all the latent heat.

Acknowledgments

This research was supported by the Advanced Research Projects Agency - Energy (ARPA-E) under Award DE-AR0000530 and the Center for Environmental Energy Engineering (CEEE).

References

[1] Al-Abidi AA, Bin Mat S, Sopian K, Sulaiman MY, Mohammed AT. CFD applications for latent heat thermal energy storage: a review. Renew Sustain Energy Rev 2013;20:353–63. doi:10.1016/j.rser.2012.11.079.

[2] Jin X, Hu H, Shi X, Zhou X, Zhang X. Comparison of two numerical heat transfer models for phase change material board. Appl Therm Eng 2018;128:1331–9. doi:10.1016/j.applthermaleng.2017.09.015.

[3] Eyres NR, Hartree DR, Ingham J, Jackson R, Sarjant RJ, Wagstaff JB. The Calculation of Variable Heat Flow in Solids. Philos Trans R Soc A Math Phys Eng Sci 1946;240:1–57. doi:10.1098/rsta.1946.0002.

[4] Dutil Y, Rousse DR, Salah N Ben, Lassue S, Zalewski L. A review on phase-change materials: Mathematical modeling and simulations. Renew Sustain Energy Rev 2011;15:112–30. doi:10.1016/j.rser.2010.06.011.

[5] Qiao Y, Du Y, Muehlbauer J, Hwang Y, Radermacher R. Experimental study of enhanced PCM exchangers applied in a thermal energy storage system for personal cooling. Int J Refrig 2019;102:22–34. doi:10.1016/J.IJREFRIG.2019.03.006.

[6] Dhumane R, Qiao Y, Muehlbauer J, Ling J, Aute V. Evaluating Recharge Options for Phase Change Material Storage of a Personal Conditioning System. Int. Refrig. Air Cond. Conf. Purdue. Purdue Univ. West Lafayette., 2018, p. 1–10.

[7] Merlin K, Delaunay D, Soto J, Traonvouez L. Heat transfer enhancement in latent heat thermal storage systems: Comparative study of different solutions and thermal contact investigation between the exchanger and the PCM. Appl Energy 2016;166:107–16. doi:10.1016/j.apenergy.2016.01.012.

[8] Py X, Olives R, Mauran S. paraffin/porous-graphite-matrix composite as high and constant power thermal storage material. Int J Heat Mass Transf 2001;44:2727–37.

[9] Churchill SW, Chu HHS. Correlating equations for laminar and turbulent free convection from a vertical plate. Int J Heat Mass Transf 1975;18:1323–9. doi:10.1016/0017-9310(75)90243-4.

[10] Qiao H, Aute V, Radermacher R. Transient modeling of a flash tank vapor injection heat pump system - Part I: Model development. Int J Refrig 2015;49:169–82. doi:10.1016/j.ijrefrig.2014.06.019.

[11] Laughman CR, Qiao H. On the influence of state selection on mass conservation in dynamic vapour compression cycle models. Math Comput Model Dyn Syst 2017;23:262–83. doi:10.1080/13873954.2017.1298625.

[12] Aute V, Radermacher R. Standardized Polynomials for Fast Evaluation of Refrigerant Thermophysical Properties. Int. Compress. Eng. Refrig. Air Cond. High Perform. Build. Conf., 2014, p. 1–10.

[13] Gnielinski V. On heat transfer in tubes. Int J Heat Mass Transf 2013;63:134–40. doi:10.1016/j.ijheatmasstransfer.2013.04.015.

[14] Shah MM. An improved and extended general correlation for heat transfer during condensation in plain tubes. HVAC&R Res Sept 2009;15.

[15] Jung DS, Radermacher R. Prediction of pressure drop during horizontal annular flow boiling of pure and mixed refrigerants. Int J Heat Mass Transf 1989;32:2435–46. doi:10.1016/0017-9310(89)90203-2.

[16] Hong KT, Webb RL. Calculation of Fin Efficiency for Wet and Dry Fins. HVAC&R Res 1996;2:27–41.

[17] Kim N-H, Yun J-H, Webb RL. Heat Transfer and Friction Correlations for Wavy Plate Fin-and-Tube Heat Exchangers. J Heat Transfer 1997;119:560–7. doi:10.1115/1.2824141.

[18] Thomas H. Kuehn, James W. Ramsey JLT. Thermal Environmental Engineering. vol. 188. 1998.

[19] Wang F, Maidment G, Missenden J, Tozer R. The novel use of phase change materials in refrigeration plant. Part 2: Dynamic simulation model for the combined system. Appl Therm Eng 2007;27:2902–10. doi:10.1016/j.applthermaleng.2005.06.009.